Supplementary Information for

Vapor and heat dual-drive sustainable power for portable electronics in ambient environment

Jiaxin Bai,[a] Yajie Hu,[b] Tianlei Guang,[a] Kaixuan Zhu,[a] Haiyan Wang,[b] Huhu Cheng,[ab] Feng Liu[c] and Liangti Qu*[ab]

[a]State Key Laboratory of Tribology, Department of Mechanical Engineering, Tsinghua University, Beijing, 100000, China.

[b]Key Laboratory of Organic Optoelectronics & Molecular Engineering, Ministry of Education, Department of Chemistry, Tsinghua University, Beijing, 100000, China.

[c]State Key Laboratory of Nonlinear Mechanics, Institute of Mechanics, Chinese Academy of Sciences, Beijing 100190, China.

E-mail: lqu@mail.tsinghua.edu.cn (L. Qu)

This supplementary information file includes:

Figs. S1 to S35
Tables S1 to S3
Video S1
Supplementary Notes S1 to S3

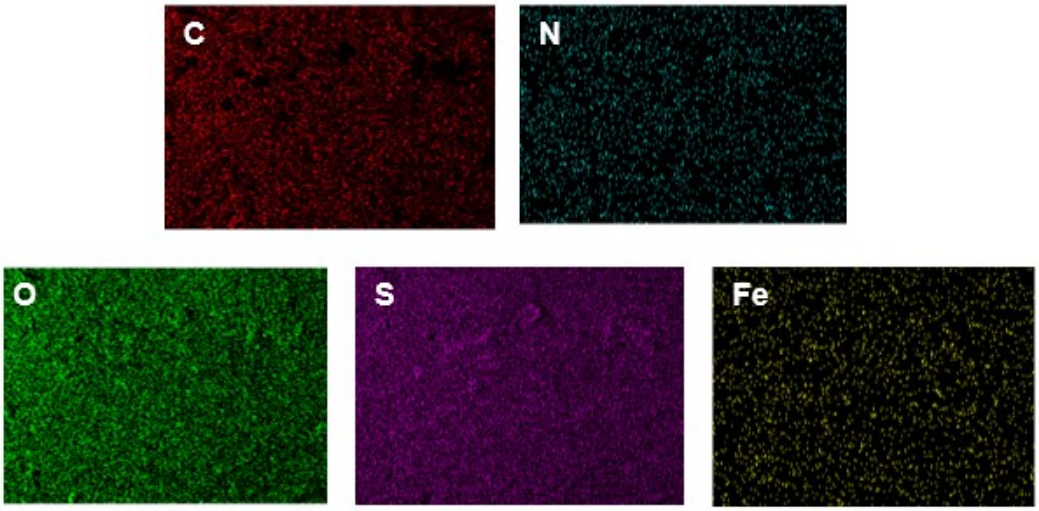

Fig. S1 Element mapping images of PSSA-PEDOT:PSS-$FeCN^{4-/3-}$ film.

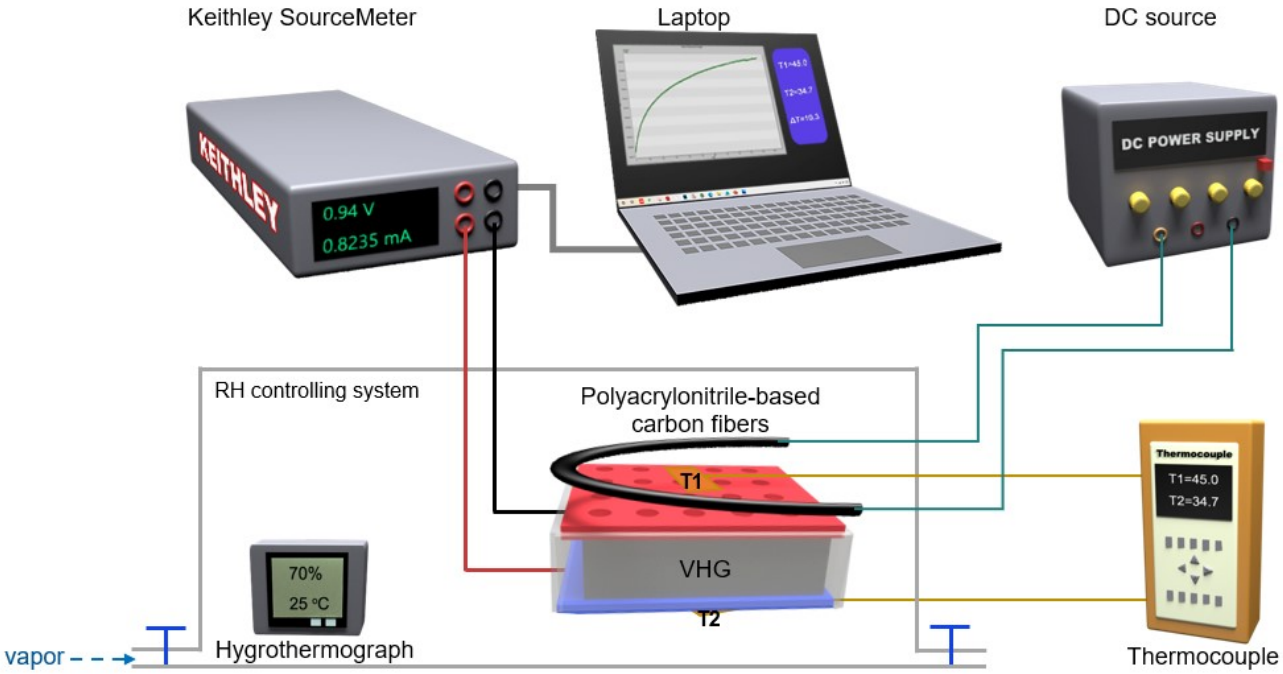

Fig. S2 Experimental setup of the power generation process.

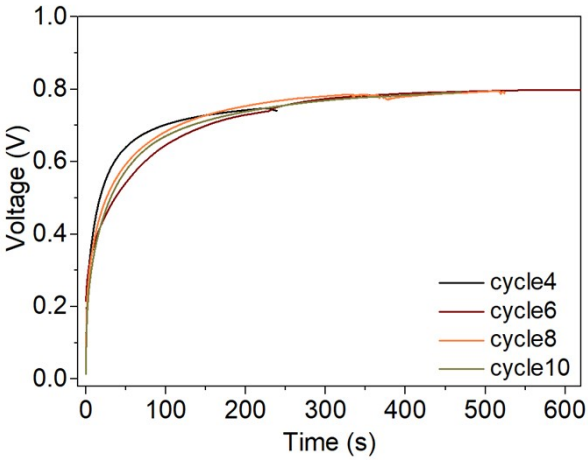

Fig. S3 Repeatable power generation of a VHG. The device was dried for 12 hours after every cycle.

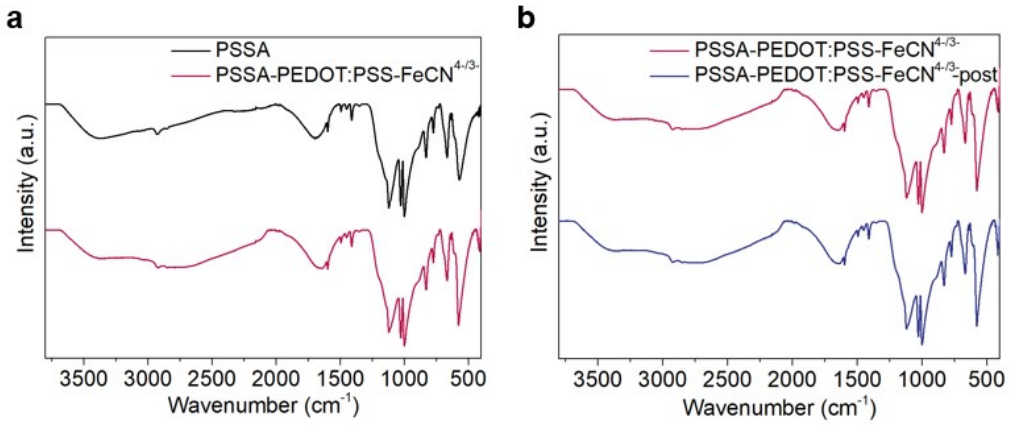

Fig. S4 (a) FTIR curves of PSSA and PSSA-PEDOT:PSS-FeCN$^{4-/3-}$ film. (b) FTIR curves of PSSA-PEDOT:PSS-FeCN$^{4-/3-}$ film before and after the cycling performance test.

The Fourier transforminfrared spectroscopic (FTIR) results of the PSSA-PEDOT:PSS-FeCN$^{4-/3-}$ film before and after the cycling investigation show identical patterns, suggesting that detectable change of functional groups during the whole process is excluded.

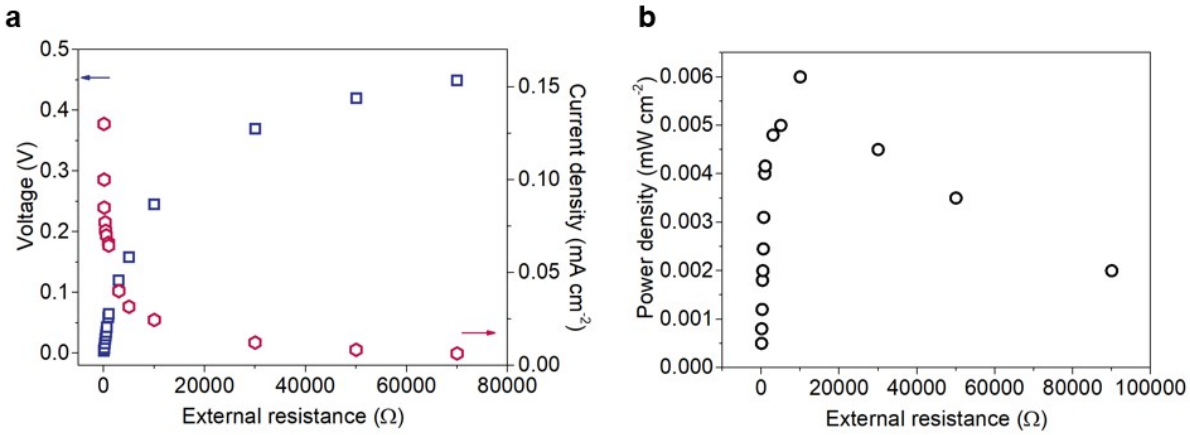

Fig. S5 Electric output of VHG based on PSSA film with different electrical resistance as load under 70%RH. (a) Dependence of current density, voltage output and (b) power density on electrical resistance of the external circuit.

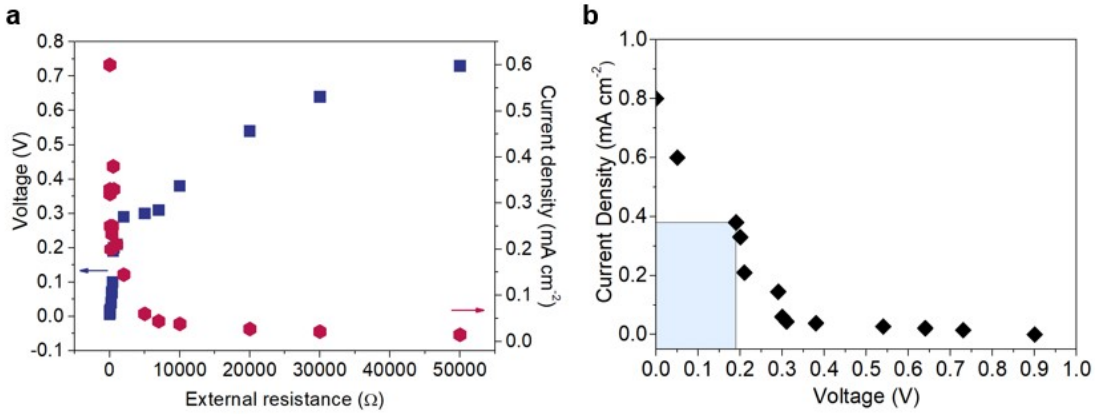

Fig. S6 Electric output of VHG based on PSSA-PEDOT:PSS-$FeCN^{4-/3-}$ film with different electrical resistance as load under 70%RH, ΔT=10 ºC. (a) Dependence of current density and voltage on electrical resistance of the external circuit. (b) The current density-voltage curve of a VHG.

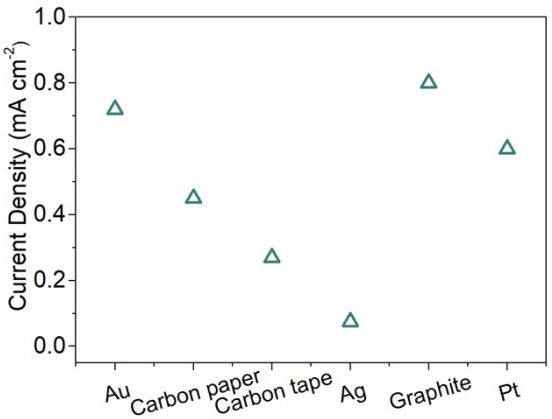

Fig. S7 I_{sc} of the VHG based on different electrodes.

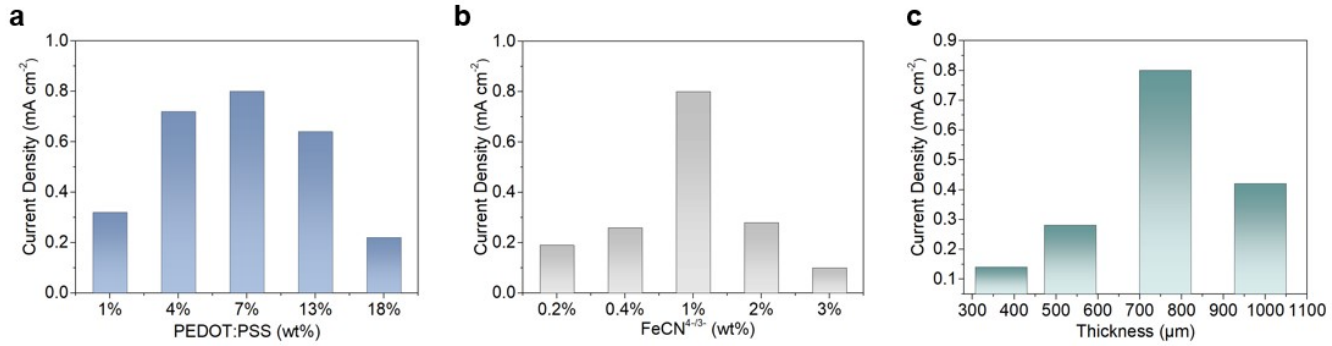

Fig. S8 The dependence of I_{sc} on different content (wt.%) of (a) PEDOT:PSS, (b) $FeCN^{4-/3-}$ in PSSA-PEDOT:PSS-$FeCN^{4-/3-}$ film. (c) I_{sc} of VHG based on PSSA-PEDOT:PSS-$FeCN^{4-/3-}$ film with different film thickness under 70% RH, ΔT=10 °C.

The I_{sc} of VHG gradually enhances with the thickness of ternary hybrid increasing from 350 μm to 740 μm, and decreases with a further increase in thickness. When the film is too thin, VHG adsorbs less water molecules from vapor and subsequently dissociates inadequate mobile H^+ ions and the temperature difference in a VHG is difficult to hold persistent resulting in a lower current output. When the hybrid film is too thick, the migration pathway for ions is too long, impeding ion transport. In conclusion, a considerable I_{sc} of the ternary hybrid is optimized at a ratio of PSSA (92 wt%) : PEDOT:PSS (7 wt%) : $FeCN^{4-/3-}$ (1 wt%) with a film thickness of about 740 μm.

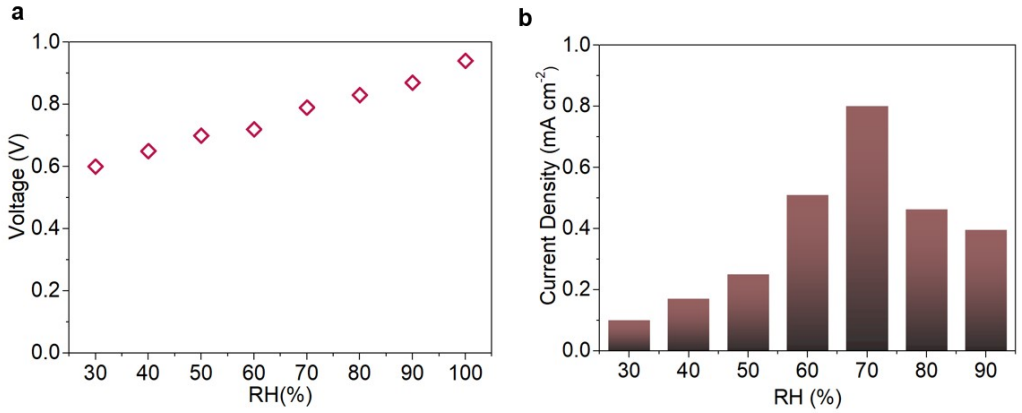

Fig. S9 (a) V_{oc}, (b) I_{sc} of VHG under different RH (50–100%) at ΔT=10 °C.

The dependence of V_{oc} on RH (50%–100%) demonstrates that power generation is directly related to the hydration level of PSSA-PEDOT:PSS-$FeCN^{4-/3-}$ film exposed to humid environment. The I_{sc} of VHG is visibly increased with the rise of RH approaching a considerable value of about 0.8 mA cm^{-2} at RH = 70%. As the rise of RH, the thermal conductivity of PSSA-PEDOT:PSS-$FeCN^{4-/3-}$ film will increase with

the water content because the thermal conductivity of water (≈0.6 W m^{-1} K^{-1}) is higher than typical polymers (Fig. 3d).[1,2] The increased thermal conductivity adverses to maintaining the temperature gradient along VHG. Therefore, the I_{sc} of VHG slightly decline at RH=70%–90%.

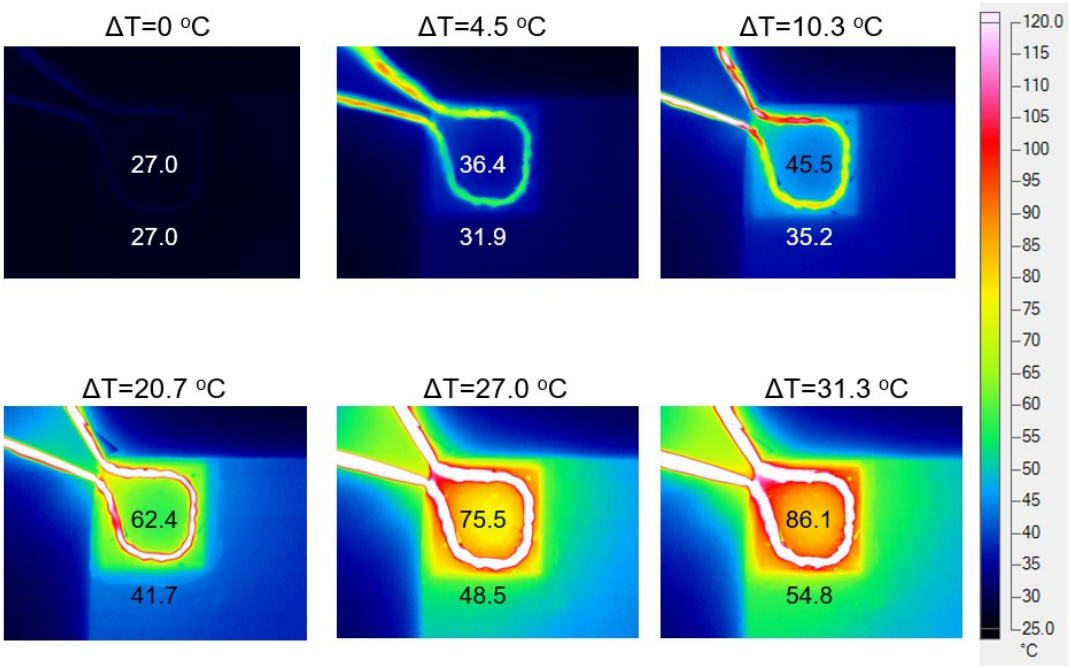

Fig. S10 The infra-red images of VHG under different temperature difference.

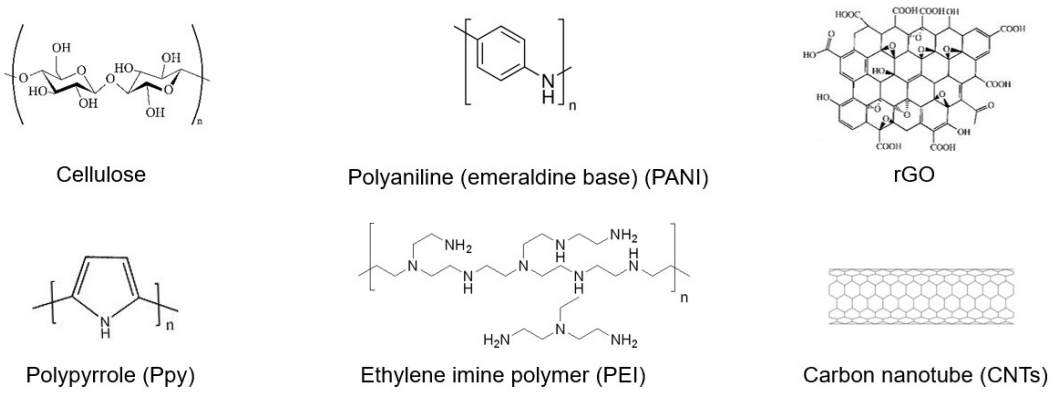

Fig. S11 Chemical formulas of additives in PSSA matrix in Fig. 2d.

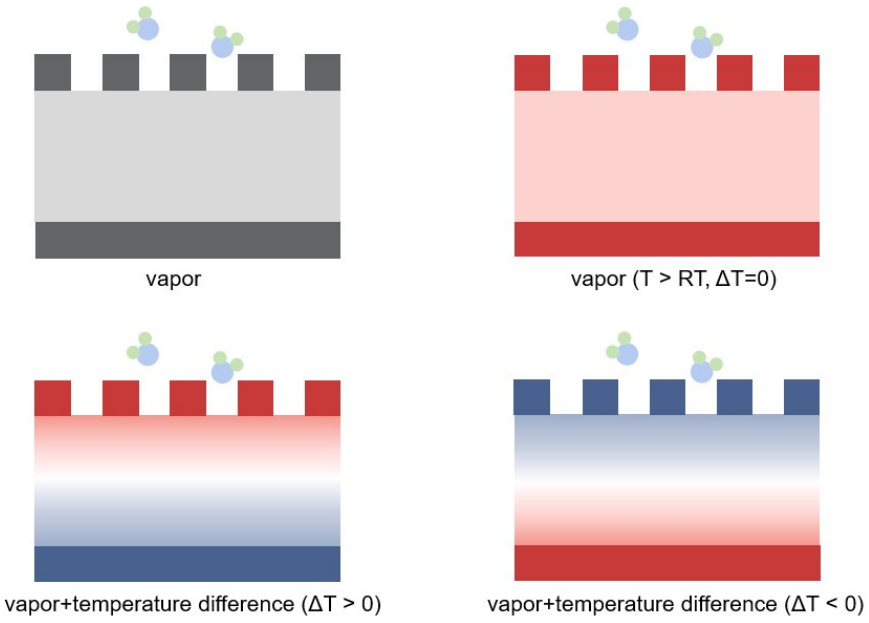

Fig. S12 The scheme of VHG in the experiments of Fig. 2e. Red represents the electrode at hot side, and blue denotes the electrode at cold side.

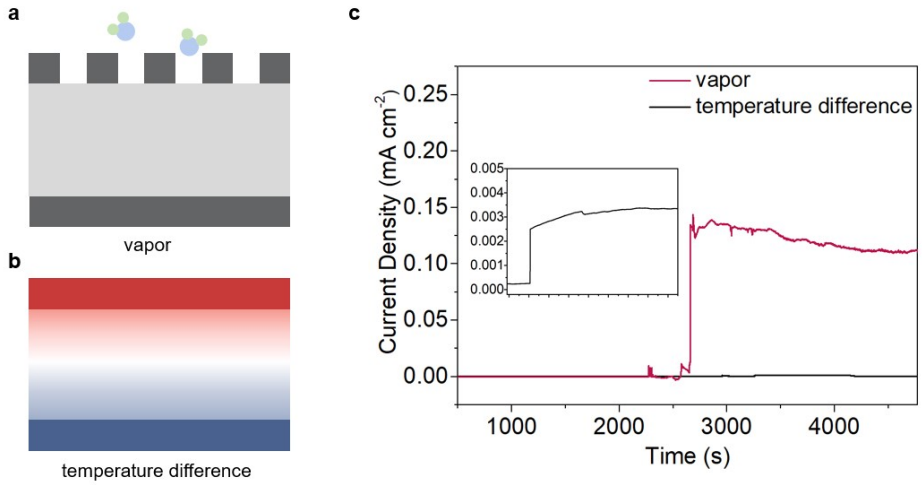

Fig. S13 The scheme of VHG under (a) vapor and (b) temperature difference. (c) I_{sc} of VHG in response to vapor and temperature difference, respectively.

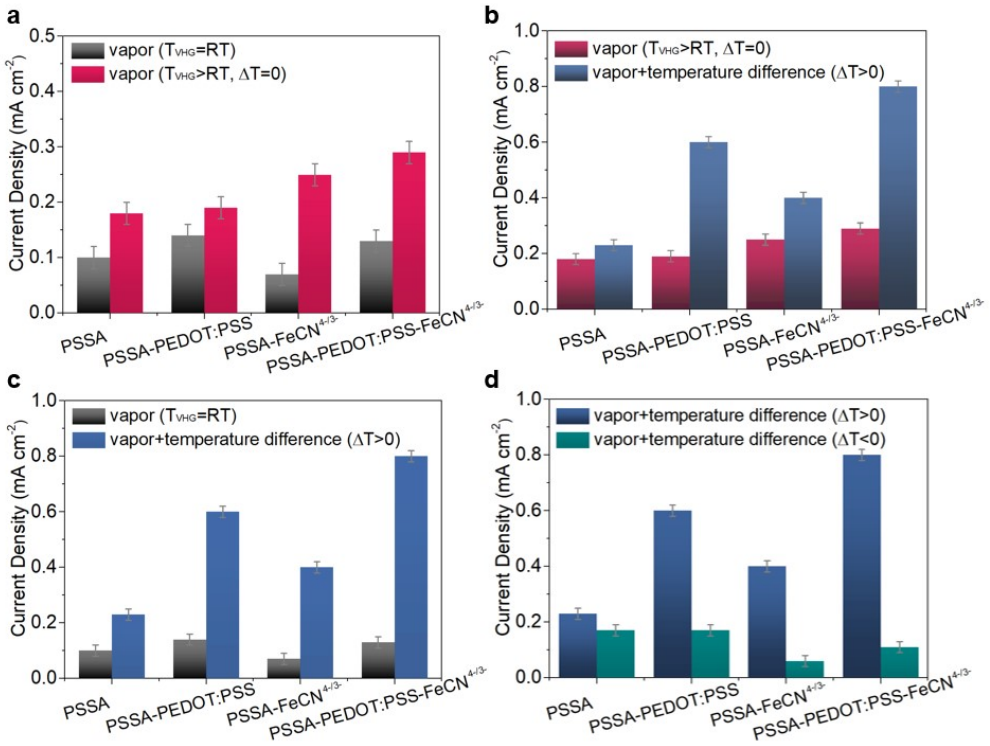

Fig. S14 I_{sc} of PSSA, PSSA-PEDOT:PSS, PSSA-FeCN$^{4-/3-}$ and PSSA-PEDOT:PSS-FeCN$^{4-/3-}$ film upon (a) vapor only (T_{VHG}=RT) and vapor with uniform heating (T_{VHG} > RT, ΔT=0), (b) vapor with uniform heating (T_{VHG} > RT, ΔT=0) and vapor+temperature difference (ΔT > 0), (c) vapor only (T_{VHG}=RT) and vapor+temperature difference (ΔT > 0), (d) vapor+temperature difference (ΔT > 0 and ΔT < 0).

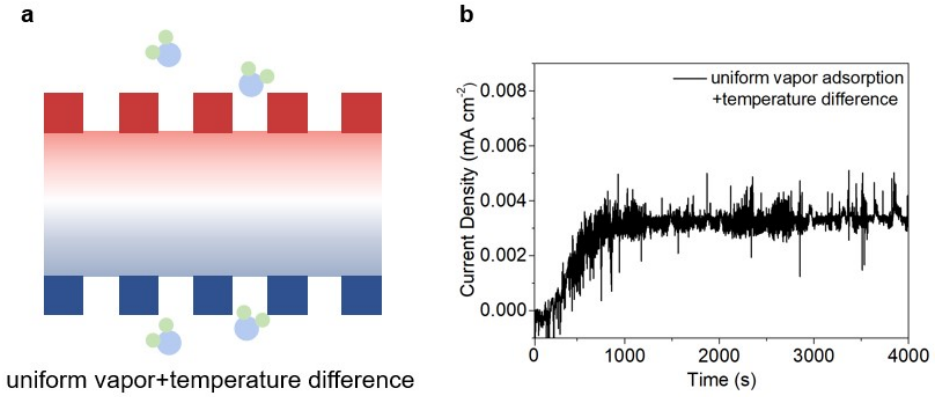

Fig. S15 (a) The scheme and (b) I_{sc} of VHG with two opposite porous electrodes under uniform vapor and temperature difference.

Table S1 The comparison information of different water adsorption enabled electric generation systems

Materials		Electrodes	Voltage (V)	Current density ($mA\ cm^{-2}$)	Power density ($\mu W\ cm^{-2}$)	Reference
Graphene	g-GOF	Au	0.04	0.010	0.42	3
	IPMEG	rGO	0.18	0.001	0.10	4
	GO film-1	steel@Au	0.70	0.025	-	5
	GO film	Ag	0.70	0.003	27	6
	a-GOM	Au	0.45	0.001	0.0184	7
	h-3D-GO	Au/Ag	1.50	4.3E-5	32000	8
	GON	Al	0.04	3.000	12	9
	g-3D-GO	Al	0.26	3.200	940	10
Other carbon-based materials	PCF	C	0.07	6E-7	-	11
	Cellulose	-	0.11	0.022	0.0003	12
	CNFs	copper	0.65	0.55	-	13
Polymer	PSSA	steel@Au	0.80	0.100	17	14
	PPy foam	Au	0.06	0.010	0.69	15
	HCl/ PVA	CNT	0.35	0.660	47	16
	PVA/GO	FTO	0.85	0.009	1.36	17
	GO/PAAS	Au/Ag	0.60	0.001	0.07	18
	PSSA+PVA	Ag NWs	0.60	0.100	7.9	19
	PSSA/PVA	carbon tape	0.95	0.001	5.5	20
	PSSA/R	Au	0.92	0.57	88	21
Metallic oxide	TiO_2	Ag NW	0.50	0.008	4	22
This work	PSSA-PEDOT:PSS-$FeCN^{4-/3-}$	graphite	0.94	0.840	72	vapor+ temperature difference
			0.86	0.130	6.0	vapor

Table S2 The comparison information of different thermoelectric generation systems

Materials	Seebeck coefficient (mV K^{-1})	Figure-of-merits	Power factor (mW m^{-1} K^{-2})	Temperature difference (K)	Voltage of per unit (V)	Number of the unit	Integrated voltage (V)	Reference
AHGA	12.6	0.85	1.80	9.5	0.10	8	1.0	2
TGC	0.8	-	0.01	-	-	-	-	23
I_3^-/I^- TEC	1.0	-	-	0.8	0.01	-	-	24
$[Fe(CN)_6]^{4-}/[Fe(CN)_6]^{3-}$	17.0	-	-	8.0	0.10	25	2.2	25
PANI:PAAMPSA:PA	8.1	1.04	1.60	3.0	0.05	-	-	1
SiO_2-PANI:PAAMPSA:PA	17.9	3.74	5.99	1.8	0.04	-	-	26
$[Fe(CN)_6]^{4-}/[Fe(CN)_6]^{3-}$	3.7	0.40	-	50.0	0.20	20	3.1	27
$[Fe(CN)_6]^{4-}/[Fe(CN)_6]^{3-}$	1.3	-	-	106	0.14	15	2.1	28
$[Fe(CN)_6]^{4-}/[Fe(CN)_6]^{3-}$	4.2	-	-	18.0	0.12	50	3.5	29
I_3^-/I^-	2.0	0.01	0.01	30.0	0.06	-	-	30
CNTs	1.6	-	-	72.0	0.09	-	-	31
Li^+/Li	2.1	-	-	35.0	0.08	-	-	32
$Co^{II/III}$	2.0	-	-	70	-	-	-	33
CNTs	1.4	-	-	60.0	0.07	-	-	34
graphene	1.4	-	-	20.0	0.03	-	-	35
rGO	1.4	-	-	31.0	0.05	-	-	36
$[Fe(CN)_6]^{4-}/[$	1.4	-	-	51.4	0.07	-	-	37

$Fe(CN)_6]^{3-}$								
$[Fe(CN)_6]^{4-}$/[$Fe(CN)_6]^{3-}$	1.4	-	-	81.0	-	28	2.0	38
PEDOT:PSS	0.8	0.25	0.04	10.0	-	54	-	39
PEDOT:PSS	0.4	0.42	0.50	-	-	-	-	40
$[Fe(CN)_6]^{4-}$/[$Fe(CN)_6]^{3-}$	1.2	-	-	5.3	0.02	118	1.0	41
I_3^-/I^-	1.9	-	-	10.0	0.02	100	0.8	42
Cellulose	24.0	-	1.15	5.5	0.12	-	-	43
PVDF-HFP	14.0	-	-	6.0	0.10	36	1.0	44
PVA-NaOH	37.61	-	-	1	0.02	6	0.2	45
$[Fe(CN)_6]^{4-}$/[$Fe(CN)_6]^{3-}$	2.9	-	0.06	4.1	0.06	-	-	46
$[Fe(CN)_6]^{4-}$/[$Fe(CN)_6]^{3-}$	1.4	-	-	15.0	0.02	-	-	47
CNTs	0.068	0.007	14	60.0		60	0.1	48
This work	30.0	0.19	0.05	10	0.94	6	6.7	vapor+ temperature difference
	7.1	0.025	0.006	10	0.01	-	-	temperature difference

The Seebeck coefficient (S_e) value can be calculated from the slope of open-circuit voltage vs. ΔT plots.

The figure of merit

$$Z = \frac{{S_e}^2 \delta}{k} \quad (1)$$

which depends on the S_e, electrical conductivity (δ), and thermal conductivity (k)[27].

The ionic power factor ${PF_i} = {S_e}^2 \sigma_i$, where σ_i are ionic conductivity[2].

As shown in Table S2, tens or hundreds thermoelectric units have been integrated to achieve about 1 V in reported researches. In this work, six VHGs can reach up to 6.7 V, exhibiting excellent potential for further applications in real natural environment.

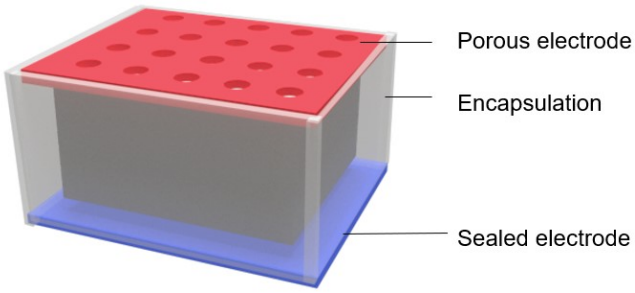

Fig. S16 The scheme of a VHG for test.

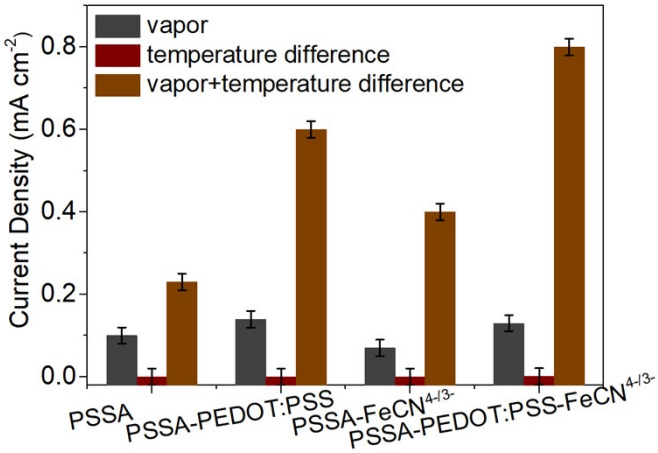

Fig. S17 I_{sc} of PSSA, PSSA-PEDOT:PSS, PSSA-$FeCN^{4-/3-}$ and PSSA-PEDOT:PSS-$FeCN^{4-/3-}$ film upon vapor only, temperature difference only and vapor+temperature difference.

The proposed process of electricity generation in a VHG could be described as follows. (1) Given different hydration level between two sides of PSSA-PEDOT:PSS-$FeCN^{4-/3-}$ film under vapor, directional transport of H^+ ions will spontaneously realize charge separation and induce an electric output. In this vapor-induced process, when a temperature difference occurs on the VHG, H^+ ion dissociation will be improved near hot electrode.[2] Thus, the gradient distribution of H^+ ions induced by vapor adsorption could be further enhanced to drive more H^+ ions migrating. Moreover, H^+ ion migration will be facilitated under relatively higher temperature.[25] (2) On the other hand, in the temperature difference induced process, the H^+ ions will tend to diffuse from the hot side to the cold side dominated by the Soret effect. The ion

thermodiffusion induced by temperature difference will also be improved by water penetration under vapor accordingly.[1] Thereupon, current will be enhanced because significantly increased charges passing through per unit time.

In consequence, both vapor adsorption and temperature difference are play significant roles in another effect, respectively. These promotion on their individual effects synergistically achieve increased carriers and abundant driving force for efficient H^+ ion migration, accordingly enhancing power generation beyond a simple sum of the two effects.

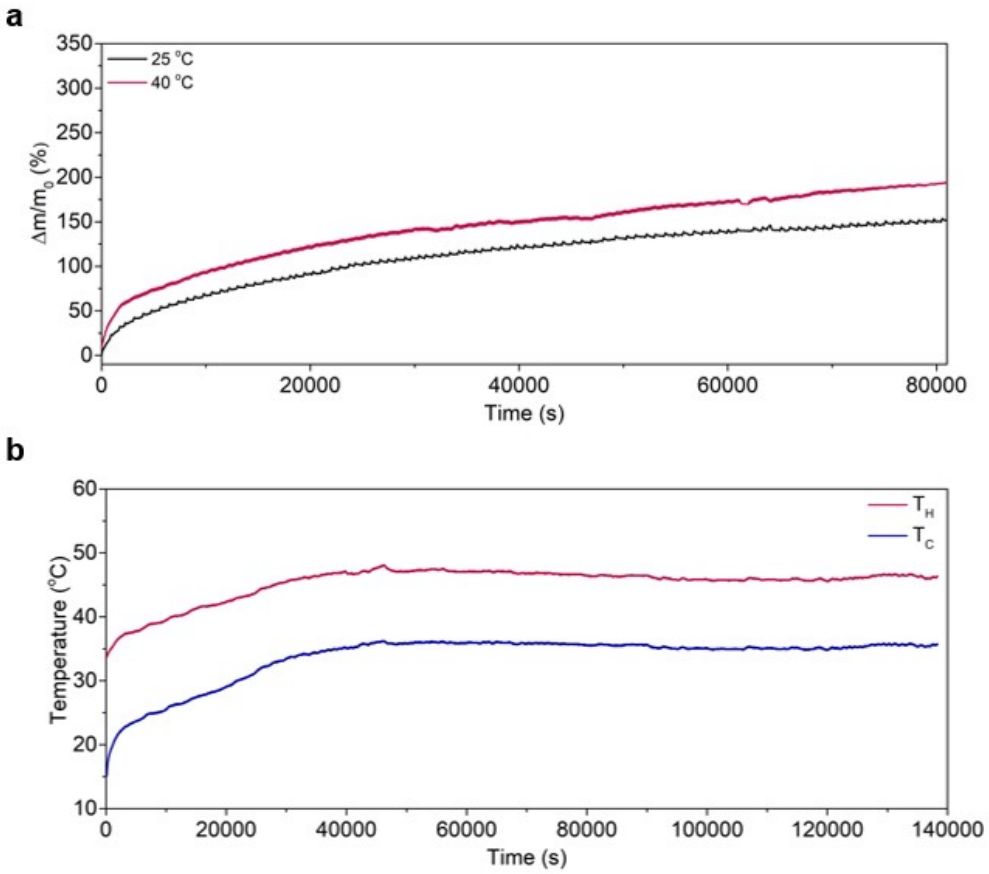

Fig. S18 (a) The mass change of VHG by water molecule adsorption versus time under 70% RH at 25 °C and 40 °C. (b) The real-tme temperature of electrodes. T_H: the temperature of the electrode at hot side. T_C: the temperature of the electrode at cold side.

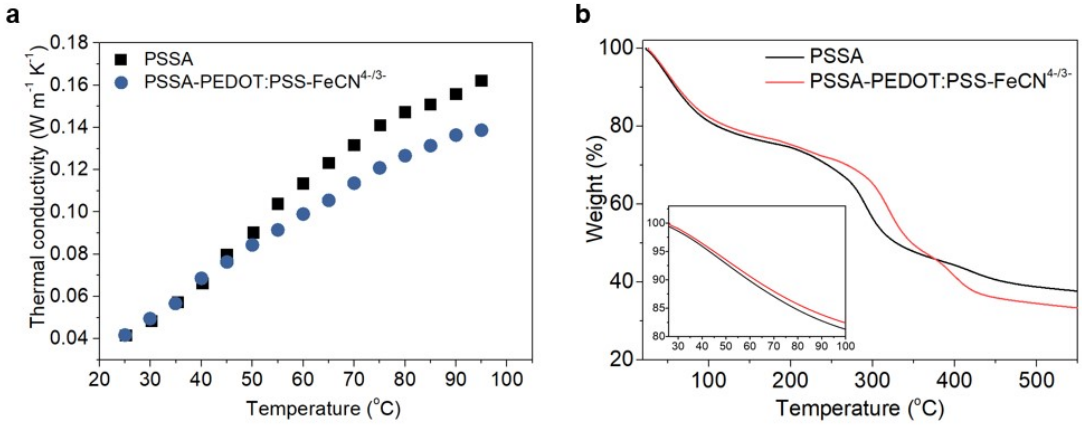

Fig. S19 (a) Thermal conductivity and (b) thermogravimetry curves of PSSA and PSSA-PEDOT:PSS-$FeCN^{4-/3-}$ film.

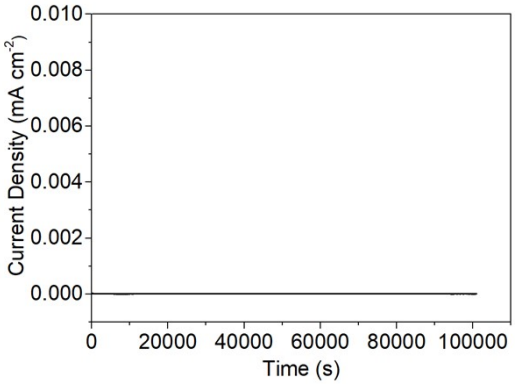

Fig. S20 I_{sc} of VHG under the environment without vapor and temperature difference.

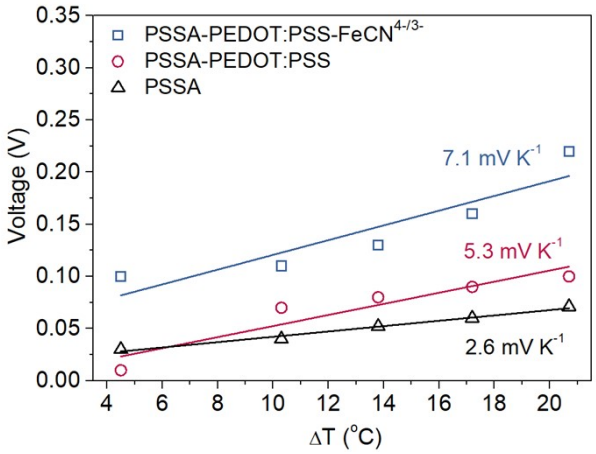

Fig. S21 Voltage of VHG as a function of ΔT.

The open-circuit voltages show a linear relationship with the applied temperature difference, and the corresponding S_e values are obtained from the slopes of these lines. A positive ionic Seebeck coefficient declares a p-type thermodiffusive thermopower. The S_e value for the pristine PSSA is 2.6 mV K^{-1}, which increases significantly to 7.1 mV K^{-1} in ternary hybrid of PSSA-PEDOT:PSS-$FeCN^{4-/3-}$.

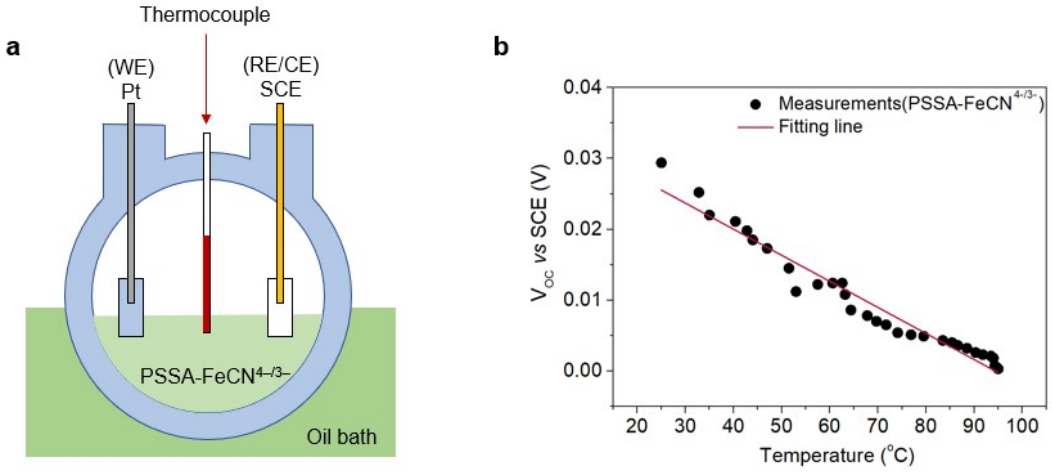

Fig. S22 (a) Isothermal three-electrode system for PSSA-FeCN$^{4-/3-}$. Platinum is served as work electrode (WE), while saturated calomel electrode (SCE) is used as reference electrode (RE) and counter electrode (CE). (b) V_{oc} vs. SCE with the dependent of temperature in an isothermal three-electrode system.

We used an isothermal three-electrode system to determine the temperature coefficient of FeCN$^{4-/3-}$. Temperature coefficient relative to SCE extracted by linear fitting is –0.37 mV K^{-1}. Note that the SCE itself has a temperature coefficient of –0.47 mV K^{-1},[49] therefore the temperature coefficient of FeCN$^{4-/3-}$ is –0.84 mV K^{-1}. The result is in good agreement with the previously reported value.[27,41]

In electrochemistry, the temperature dependence of the standard electrode potential (E_0), as an isothermal quantity, is referred as "temperature coefficient", which is defined as $\alpha_R = dE_0/dT$, where a_R is a thermodynamic property. For a redox reaction $O + ne^- \leftrightharpoons R$, where the oxidized species O is converted into the reduced species R, the temperature coefficient is $a_R = (s_R - s_O)/nF$, where s_O and s_R are partial molar entropies of the species O and R, respectively, and F is the Faraday constant. In a thermogalvanic cell under a temperature difference, the redox reaction contribution to the measured voltage is $V_{T_H} - V_{T_C} = a_R(T_H - T_C)$, which means that the sign of a_R is opposite to the sign convention of S_e.[25]

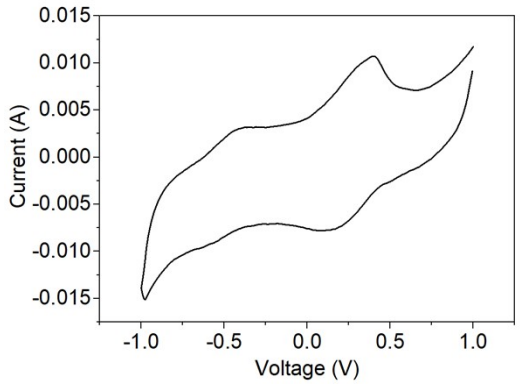

Fig. S23 Cyclic voltammetry curve scanned at 50 mV s^{-1} for PSSA-$FeCN^{4-/3-}$.

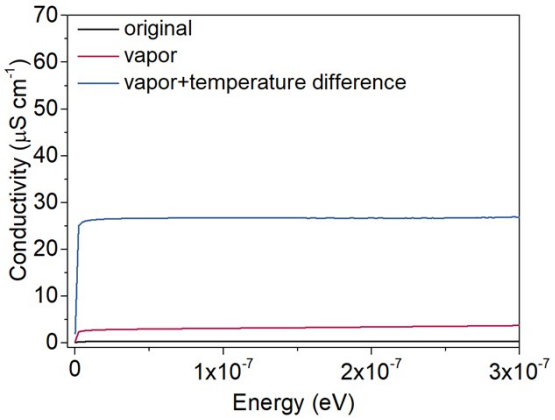

Fig. S24 The dependence of conductivity in PSSA film on vapor (RH=70%) and temperature difference (ΔT=10 °C), respectively.

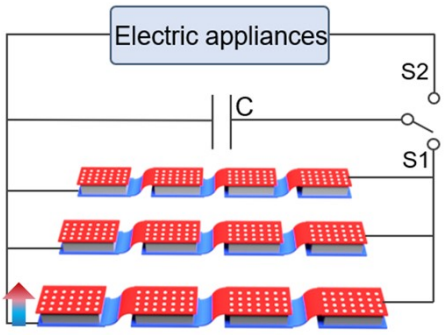

Fig. S25 The circuit diagram for applications in Fig. 5a, b and Fig. 6d, g. S1: VHGs in series-parallel connection charging for a capacitor. S2: accumulated energy in the capacitor powering commercial electronics.

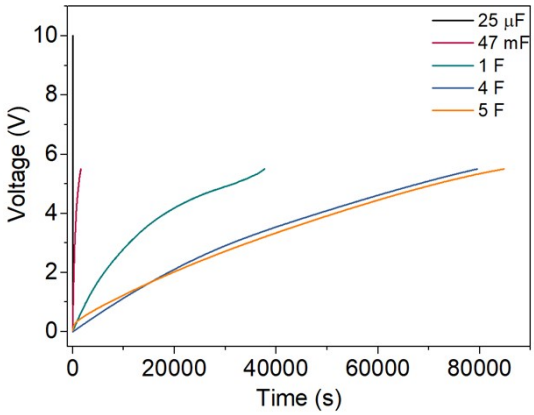

Fig. S26 Voltage-time curves of commercial capacitors charged by 12 VHG units connected in series and parallel.

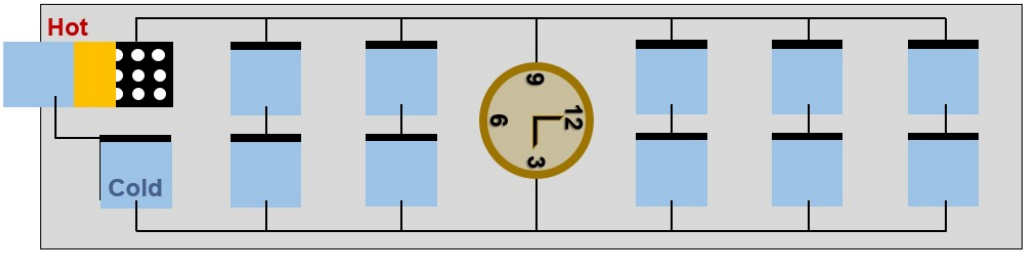

Fig. S27 The circuit diagram for a self-powered electronic watch under working condition.

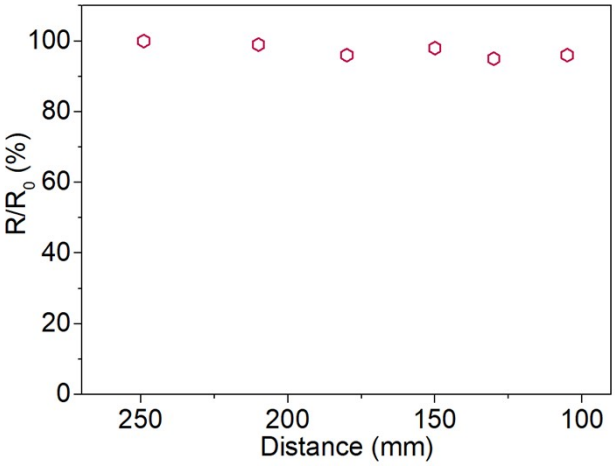

Fig. S28 Resistance retention as a function of distance between the ends of the integrated VHGs during the cyclic bending test.

It demonstrates the mechanical reliability of VHG by measuring specific value of the resistance after bending (R) to the initial resistance (R_0) under different bending conditions. The R/R_0 remains 90% when the distance of two end changes ~150 mm (insert of Fig. 6e).

Supplementary note 1

To quantify ion concentration dependence of current and voltage, kinetic Monte Carlo method is used to study ions movement inside polymer network. The ion concentration distribution C_{ion} in calculation is given as: $C_{ion}(z) = gz + C_h$, where z is the coordinates along z direction ranges from 0 to l_z corresponding to bottom and top of simulation box, g represent ion concentration gradient, and C_h is a uniform ion concentration background. Here two different ion concentration increasing scenario are considered: first, only the magnitude of ion concentration gradient g is increased and $C_h = 0\ nm^{-3}$; second, only the uniform ion concentration background C_h is increased with g unchanged. In Fig. S29, the obtained voltage and current evolution with respect to ion pair number is shown. It presents that no matter in which way current increases linearly with respect to ion pair number. However, in the first scenario voltage increase as much as current, while voltage slightly decreases in the second one. In reality, the ion concentration increasing manner should be somewhere between those two, and thus a remarkable current enhancement and relative small voltage variation could be expected. These calculated results indicate that voltage is mainly related to ion concentration gradient, while current will be affected by movable ion migration. Therefore, the current of VHG could be enhanced by applied temperature difference.

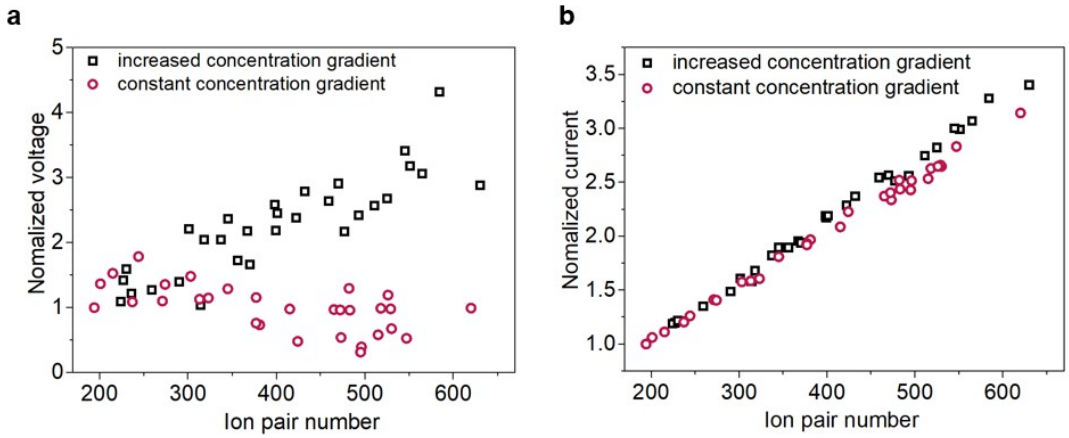

Fig. S29 The evolution of nomalized (a) voltage and (b) current with respect to ion pair number in simulation box for two different scenarios are compared, where black dots represent the first scenario that only the magnitude of ion concentration gradient is increased while red dots represent the second one that only the uniform ion concentration background is increased without changing its gradient.

As shown in Fig. 3h, the remarkable current enhancement is closely related to the high temperature at the top. Generally, there are two possible ways to increase current, the first way is to accelerate ions movement and the second one is to increase ions density. High temperature at the top could instinctively connect to the first way. However, the problem here is that 20 °C temperature difference (20 °C to 40 °C) could lead to a quadruple enhancement in current, which cannot be explained by Arrhenius equation $D = Ae^{\frac{-Q}{K_B T}}$, where D is the diffusion rate, A is pre-exponential factor, Q is activation energy for diffusion, K_B is Boltzmann constant, and T is temperature.[50] To realize the quadruple enhancement, $Q \approx 0.6\ eV$, which is much larger than the thermal energy at room temperature $K_B T = 0.026\ eV$, and ions could barely move in this situation. Therefore, current enhancement should be largely contributed by the increasing ion concentration. In fact, it origins from the upward absolute water content in air at high temperature with the given relative vapor, since it gives more chance for water adhering and entering into polymer network and therefore more ion pairs could be dissociated. However, with further temperature rise, entropy takes over and eventually at 100 °C all water evaporates. It could postulate maximum vapor in network occurs at medium temperature. In Fig. S30, the general water content variation in polymer network is shown, which is estimated by $min(\alpha C_w, C_{max})$, where

$$C_w = 6.14 \cdot exp(\frac{17.502 \cdot T}{240.97 + T}) \quad (2)$$

$$C_{max} = C_0 \cdot (T_c - T)^2 \quad (3)$$

and $C_0 =$ 0.02 g/kg, the unit for temperature T is Centi-degree, and $T_c = 100\,°C$. Here water content in the air C_w (Arden Buck equation)[51] and maximum water content C_{max} at given temperature T are two restricts for water content. For the former, it is assumed water content inside polymer should be comparable to C_w (α is a coefficient and set to one for facility), it limits water entering into network. The latter limit comes from entropy effect, and at 100 °C all water evaporates. The temperature dependence of water content in matrix is quite similar to that of current in Fig. 2b, and it could be used to explain the maximum current density phenomenon in experiments if the current density is proportional to ion concentration.

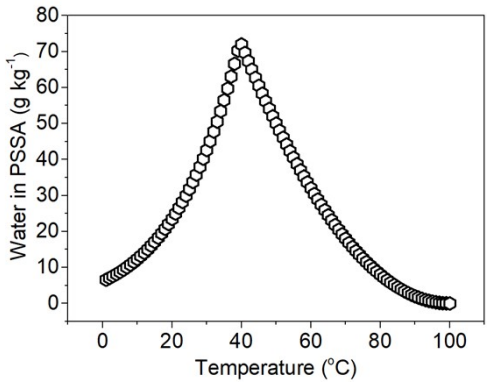

Fig. S30 The temperature dependent variation of water content in polymer network.

Although the ion concentration, which is closely related to temperature at the top, plays the most important role in this process, temperature gradient could be utilized to further enhance current. In Fig. 3h, it could be found that samples with larger temperature difference (with the temperature at the bottom is fixed at 30 °C, temperature at the top is changed, and in the middle region the linear temperature distribution is applied) show much higher current, and comparing to samples with uniform temperature it could provide additional enhancement due to the assistance from the directional heat flow (same direction as ion flow under vapor). Especially, in the case where the top and bottom temperature equal 40° and 30° respectively (near the experimental setup of maximum current density in Fig. 2b). The current under $\Delta T > 0$ shows 50% additional enhancement comparing with the current under $\Delta T = 0$, which is consistent with the increasing magnitude brought by temperature difference in experiments. Note that despite the pure rising temperature

difference could continuously increase current, combing with previous ion concentration temperature dependence, maximum current should occur at a moderate temperature, which is consistent with the experimental observation (Fig. 2b).

Based on the results of theoretical calculation, temperature at the top and temperature difference are verified as the most relevant factors for current enhancement, and their correlation with current is clarified and could be used to understand experimental results.

Calculation details

First principle calculation

Vienna Ab initio Simulation Package (VASP) is used to perform $(C_8H_8O_3S)_2$ and $(C_8H_8O_3S)_4$ structural relaxation and also energy calculation.[52] The energy cutoff and electronic self-consistent step convergence are set to be 400 eV and 10^{-4} eV , and the structure optimization requires energy change between two steps less than 10^{-3} eV/atom at least. Besides, the Perdew-Burke-Ernzerhof (PBE) exchange-correlation potential[53] is applied for all calculations. Based on the obtained uniaxial deformation energy curves (Fig. S31), the PSSA bond and angle strength could be estimated and used to derive the corresponding bond and angle spring coefficients in coarse grain MD simulations.

Coarse grain molecular dynamics (MD) simulation

Large-scale Atomic/Molecular Massively Parallel Simulator (LAMMPS)[54] is chosen to perform MD simulations, and periodic boundary condition is applied here. In calculation model, each PSSA chain $(C_8H_8O_3S)_n$ is composed by 41 coarse grain particles, and each coarse grain particle represents $(C_8H_8O_3S)_2$. Here coarse grain size is set to 5.43 Å in terms of the length of $(C_8H_8O_3S)_2$. The total energy of PSSA network is written as

$$\phi_{System} = \phi_T + \phi_\theta + \phi_{vdw}, \tag{4}$$

where the first term use harmonic potential style and is written as

$$\phi_T = \frac{1}{2}K_T(r - r_0)^2, \tag{5}$$

$$\phi_\theta = \frac{1}{2}K_\theta(\theta - \theta_0)^2,$$

where of bonds $K_T = 3.53\ eV/Å^2$, $r_0 = 5.43$ Å, $K_\theta = 163\ eV$, and $\theta_0 = 180°$, which are bond (angle) spring coefficient and equilibrium bond distance (equilibrium bond angle). Note that these parameters are

determined based on first principle calculation results. Among different PSSA chains, Lennard-Jones potential is used to describe van der Waals interaction,

$$\phi_{vdw} = 4\varepsilon[(\sigma/r)^{12} - (\sigma/r)^{6}], \tag{6}$$

where $\varepsilon = 0.2\ eV$. and $\sigma = 4.84$ Å.

2731 PSSA chains are placed in a 30×30×30 nm^3 periodic simulation box. With NVT ensemble at room temperature, the system is relaxed over 1000 ps (time step is set to 2 fs), which outputs a stable PSSA network structure and will be used as the skeleton for hydrated H^+ ion diffusion simulation based on kinetic Monte Carlo method.

Kinetic Monte Carlo simulation

N-Fold Way (NFW) algorithm is adopted to perform kinetic Monte Carlo simulations.[55–57] Here the previous prepared PSSA network structure is taken as a rigid skeleton, hydrated H^+ ion could hop to neighbor sites of PSSA network if distance is no more than 5.43 Å, and the rate of a diffusional hop is given by

$$r_D = \begin{cases} D_0 exp\left(-\dfrac{Q}{k_B T}\right) & \Delta E \le 0, \\ D_0 exp\left(-\dfrac{Q + \Delta E}{k_B T}\right) & \Delta E > 0, \end{cases} \tag{7}$$

where ΔE is energy change and $Q = 0.2\ eV$ is diffusion activation energy. The total energy of this model is given by

$$E_{tot} = \alpha \sum_{i\,=\,ions} \frac{Z_i Z_j}{r_{ij} + d_c} + \beta \cdot I_m \tag{8}$$

where the first term is used to describe the interaction between ions, and α is a scaling factor. Its only difference from coulomb potential comes from d_c, which is set to guarantee that the coulomb attraction between cations and anions when they meet on one site is small enough to be broken by kinetic energy, i.e. $k_B T$. Second term represents linear vapor intensity dependence of ion hydration energy, β is a coeffect to control its magnitude. Note that I_m is the normalized vapor intensity whose value could not be greater than

one. The values of d_c, α, and β used in this simulation are set to 1 Å, 0.01 $eV \cdot$ Å, and 0.1 eV (when $I_m = 1$), respectively.

To quantify ion concentration dependence of current and voltage shown in Fig. S29, the ion concentration distribution C_{ion} in calculation is given as $C_{ion}(z) = gz + C_h$, where z is the coordinates along z direction ranges from 0 to 300 Å. Two different ion concentration increasing scenario are considered: first, only the magnitude of ion concentration gradient g is increased (ranges from 0.000494to 0.001482 nm^{-4}) and $C_h = 0\ nm^{-3}$; second, only the uniform ion concentration background C_h is increased (from 0 to 0.0148 nm^{-3}) with g=0.000494 nm^{-4} unchanged.

In simulation, while voltage difference could be monitored directly each step and obtain its average value, current is estimated by $\Delta E/(U\tau)$, where ΔE is total energy increase during the process, U is voltage, and τ represents relaxation time. Note that τ is assumed to be independent of ion concentration, since it is mainly decided by the obstacle of kink and junction on PSSA network, which are far more frequent to meet comparing to other ions.

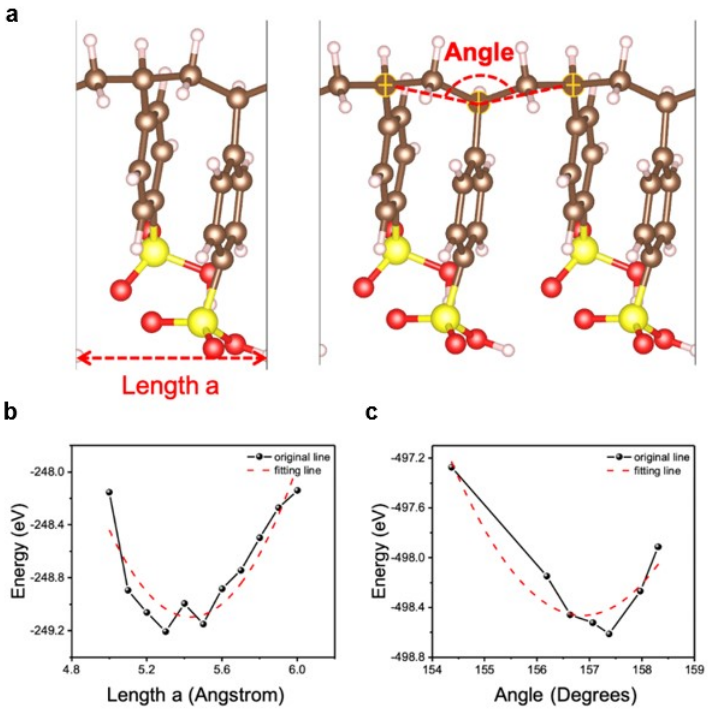

Fig. S31 First principle calculation results. (a) The structure of PSSA, where two $(C_8H_8O_3S)_2$ and $(C_8H_8O_3S)_4$ supercells are shown, and the geometrical parameters definition of length a and Angle θ are marked. With uniaxial deformation along the PSSA chain direction, energy with respect to length a and Angle θ are shown in (b) and (c), respectively.

Supplementary note 2

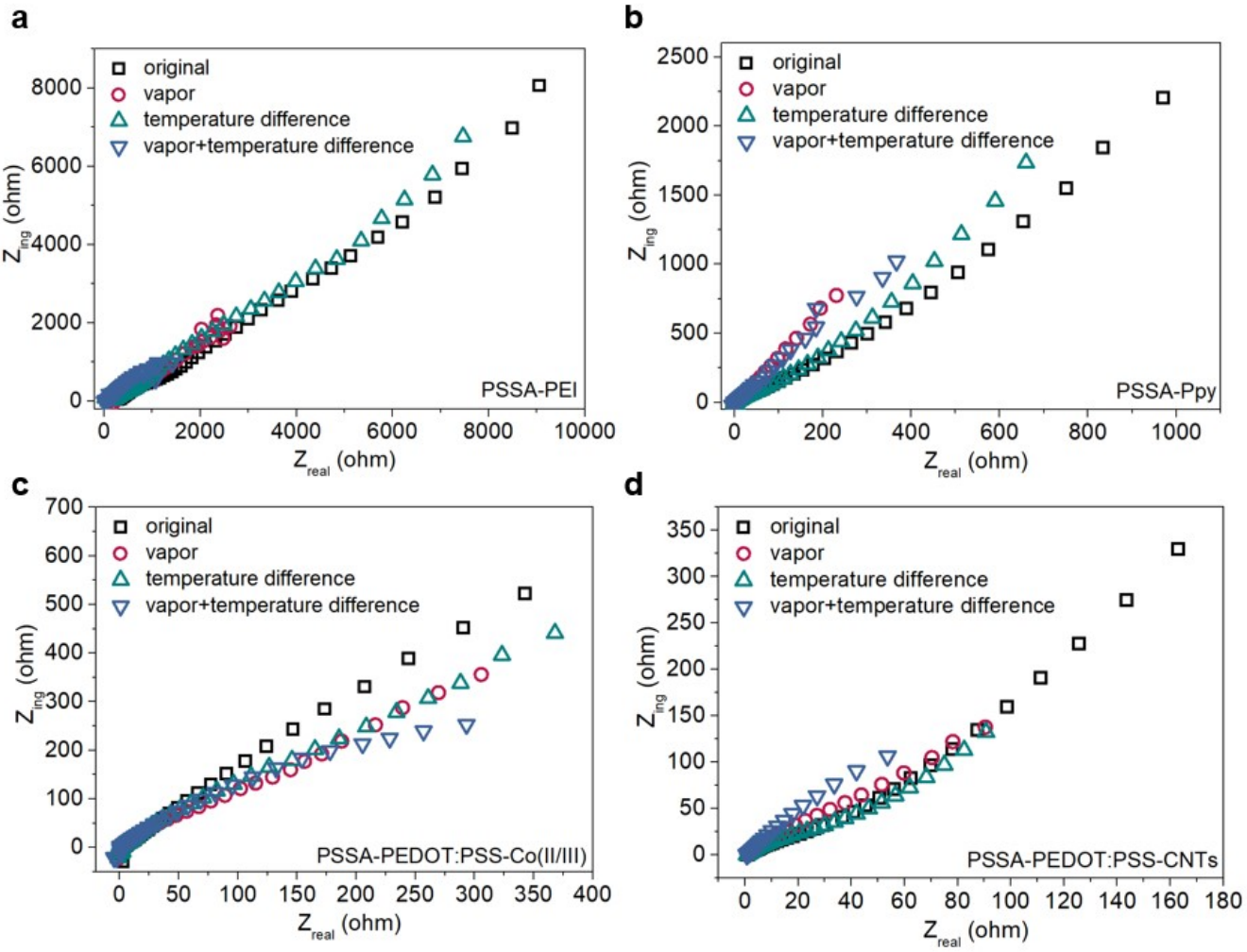

Fig. S32 The electrochemical impedance of (a) PSSA- PEI, (b) PSSA-Ppy, (c) PSSA-PEDOT:PSS-Co(II/III), (d) PSSA-PEDOT:PSS-CNTs film in response to vapor and temperature difference respectively (RH=70%, ΔT=10 °C).

Table S3 The ionic conductivity of PSSA, PSSA-PEDOT:PSS-$FeCN^{4-/3-}$, PSSA-PEI, PSSA-Ppy, PSSA-PEDOT:PSS-Co(II/III) and PSSA-PEDOT:PSS-CNTs film under vapor and temperature difference (RH=70%, ΔT=10 °C).

conductivity (μS cm^{-1})	original	vapor	vapor+temperature difference
PSSA	0.36	3.9	27
PSSA-PEDOT:PSS-$FeCN^{4-/3-}$	0.04	6.2	51
PSSA-PEI	3.6	14	36
PSSA-Ppy	34	62	89
PSSA-PEDOT:PSS-CNTs	200	130	93
PSSA-PEDOT:PSS-Co(II/III)	91	110	110

As shown in Fig. S32 and Table S3, the ion conductivity of PSSA and PSSA-PEDOT:PSS-$FeCN^{4-/3-}$ film under vapor and temperature difference show two or three orders of magnitude over that of original PSSA and PSSA-PEDOT:PSS-$FeCN^{4-/3-}$ film. It suggests that the enhanced ionic conductivity owing to H^+ ion diffusion driven by directional water adsorption and temperature difference. Although the original conductivity of the composite of PSSA with other addictives are higher than that of PSSA-PEDOT:PSS-$FeCN^{4-/3-}$ film, no significant increase occurs in the composite of PSSA with other addictives after applied vapor or temperature difference. These results indicate that ion dissociation and migration are deficient in these composite, which adverse to vapor and heat dual-drive electric generation.

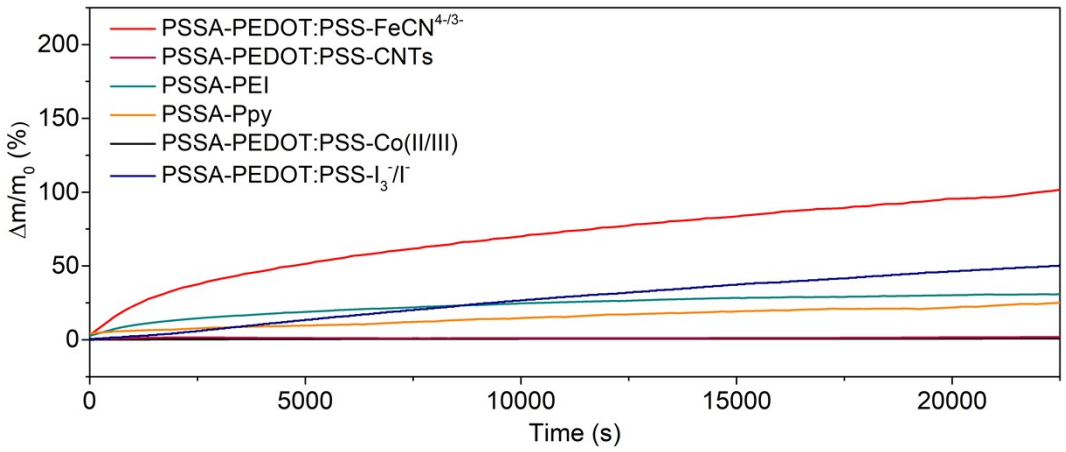

Fig. S33 The mass change of VHG based on PSSA-PEDOT:PSS-$FeCN^{4-/3-}$, PSSA-PEI, PSSA-Ppy, PSSA-PEDOT:PSS-CNTs, PSSA-PEDOT:PSS-Co(II/III), PSSA-PEDOT:PSS-I_3^-/I^- film and by water molecule adsorption versus time under 70% RH.

For thermogalvanic effect, redox couples such as cobalt tris(bipyridyl) (Co(II/III)), iodide/triiodide (I_3^-/I^-), and ferro/ferricyanide ($FeCN^{4-/3-}$) have been reported absolute temperature coefficient of a few millivolts per degree Kelvin.[25] The highest negative temperature coefficients of –4.2 mV K^{-1} was realized using the $FeCN^{4-/3-}$ redox couple in an aqueous system, which could promote the electric power.[8]

The mass change ($\Delta m/m_0 \times 100\%$) of VHG based on PSSA-PEDOT:PSS-$FeCN^{4-/3-}$ film by water adsorption increases continuously to be about 130 % at 70% RH. However, VHG based on other composite film show weak water adsorption ability, which mainly results in low electric output under vapor and temperature difference.

Supplementary note 3

1. Input energy

In the process of vapor induced electricity generation of VHG, the variation of chemical potential energy of water molecules, corresponding to the transformation from gaseous water to adsorbed water in VHG (Fig. S34), could be reasonably considered as the main energy source under vapor. The chemical potential of gaseous water and adsorbed water is μ_g and μ_a, respectively.

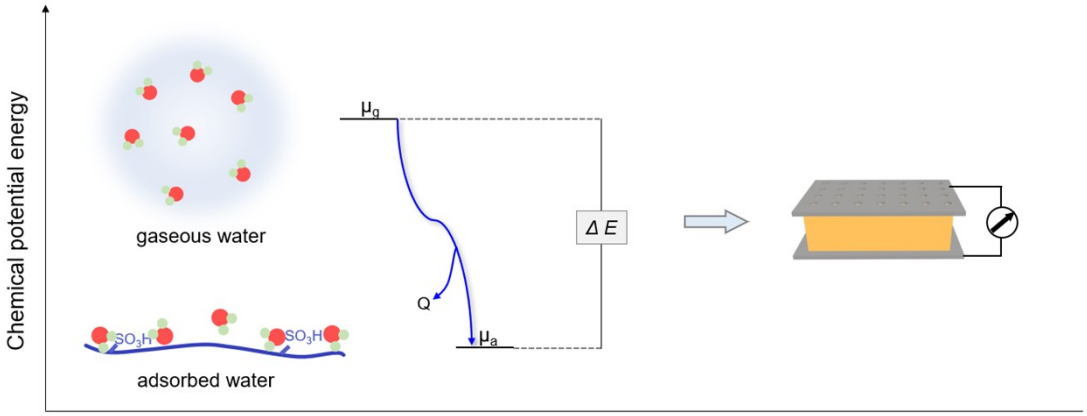

Fig. S34 Schematic illustration of energy input and conversion involved in electricity generation of VHG under only vapor. Energy input of electricity generation comes from variation of chemical potential energy of water molecules (ΔE). The μ_g and μ_a represents the chemical potential energy of gaseous water and adsorbed water, respectively. Q represents heat loss.

Water adsorption is assumed to be an isothermal and isobaric process. From thermodynamic law, the normal chemical potential μ_i is calculated as:

$$\mu_i = \left(\frac{\partial G}{\partial n_i}\right)_{T,P} \tag{9}$$

$$\mu_i = \mu_i^{\theta} + RTlna_i \tag{10}$$

where G, n_i, T, P, R, μ_i^{θ} and a_i represents Gibbs free energy, the number of moles, temperature, atmospheric pressure, ideal gas constant, standard chemical potential and activity, respectively.

In the process of water adsorption of VHG, the water molecules will spontaneously change from a free gaseous state to an adsorbed state. The Gibbs free energy variation can be considered as:

$$\Delta G = \mu_a - \mu_g < 0 \tag{11}$$

which reflects the reduction of chemical potential energy of water molecules. Therefore, VHG enables to spontaneously adsorb gaseous water in air. Thus, the maximal energy input under vapor could be estimated as:

$$\Delta G_{in} = \mu_g - \mu_a \approx RTln\frac{c_0}{c_0 - \Delta c} \tag{12}$$

where c_0 and Δc represent the concentration of water in atmospheric and the concentration variation of water, respectively. The concentration of water in atmospheric and the concentration variation of water could be estimated by the previous report.[3,10,20,58] As a result, we could appropriately calculate the maximal energy input of about 0.128 J at 298 K, 70%RH arisen from variation of chemical potential of water.

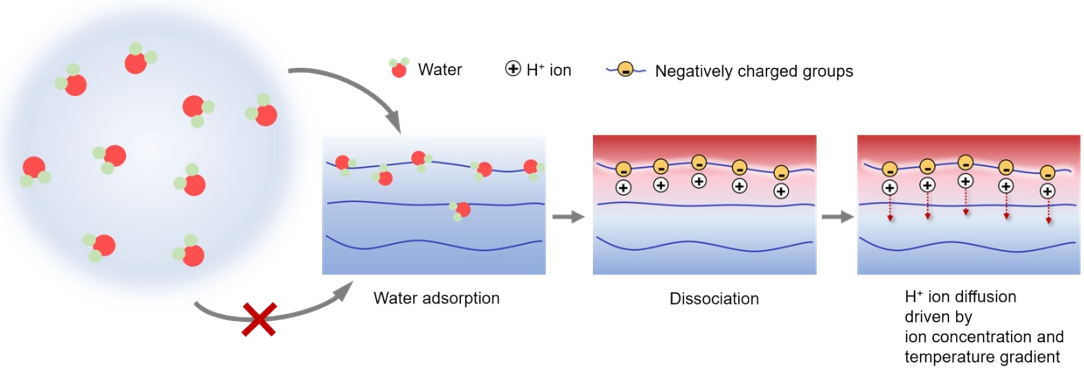

Fig. S35 Scheme of electric generation process in VHG, including water adsorption, ion dissociation and ion diffusion driven by directional vapor and temperature difference.

When a VHG contact with vapor and temperature difference, the chemical potential variation of water and heat input power (P_{heat}) is the input energy source for the energy conversion process synergistically. P_{heat} is the heat flux through the device, which can be calculated by:[27,37]

$$P_{heat} = kA\frac{\Delta T}{d} \tag{13}$$

where k is the thermal conductivity, A is the cross-sectional area, ΔT is the temperature difference between two electrodes, and d is the inter-electrode distance.[59] The applied temperature difference endows energy input (S) of 345.6 J to VHG (ΔT=10 °C).

Given different hydration level between two sides of PSSA-PEDOT:PSS-$FeCN^{4-/3-}$ film under vapor, directional transport of H^+ ions will spontaneously realize charge separation and induce an electric output. This H^+ ion migration would be further driven by temperature difference in VHG based on the Soret effect working synergistically with thermogalvanic effect of a redox couple. The increased carriers and abundant driven force for efficient H^+ ion diffusion accordingly enhance power generation (Fig. S35).

2. The energy conversion efficiency

The real output energy of VHG has been measured by connecting an optimally external resistor. The generated electricity power can be calculated as:

$$W = \int U(t)I(t)d(t) \tag{14}$$

where U, I and t are the generated voltage, current and time of producing electricity, respectively. As a result, the calculated electricity energy is about 0.02 J (70% RH) and 5.8 J (70% RH, ΔT=10 °C). Accordingly, the energy conversion efficiency ($W/\Delta G_{in}+S$) is estimated to be about 1.7% at 70% RH and ΔT=10 °C.

References

1. Z. A. Akbar, J. W. Jeon and S. Y. Jang, *Energy Environ. Sci.*, 2020, **13**, 2915–2923.
2. M. Jeong, J. Noh, M. Z. Islam, K. Kim, A. Sohn, W. Kim and C. Yu, *Adv. Funct. Mater.*, 2021, **31**, 2011016.
3. F. Zhao, H. Cheng, Z. Zhang, L. Jiang and L. Qu, *Adv. Mater.*, 2015, **27**, 4351–4357.
4. C. Yang, Y. Huang, H. Cheng, L. Jiang and L. Qu, *Adv. Mater.*, 2019, **31**, 1805705.
5. T. Xu, X. Ding, C. Shao, L. Song, T. Lin, X. Gao, J. Xue, Z. Zhang and L. Qu, *Small*, 2018, **14**, 1704473.
6. Y. Liang, F. Zhao, Z. Cheng, Y. Deng, Y. Xiao, H. Cheng, P. Zhang, Y. Huang, H. Shao and L. Qu, *Energy Environ. Sci.*, 2018, **11**, 1730–1735.
7. H. Cheng, Y. Huang, F. Zhao, C. Yang, P. Zhang, L. Jiang, G. Shi and L. Qu, *Energy Environ. Sci.*, 2018, **11**, 2839–2845.
8. Y. Huang, H. Cheng, C. Yang, P. Zhang, Q. Liao, H. Yao, G. Shi and L. Qu, *Nat. Commun.*, 2018, **9**, 4166.
9. F. Zhao, L. Wang, Y. Zhao, L. Qu and L. Dai, *Adv. Mater.*, 2016, **29**, 1604972.
10. F. Zhao, Y. Liang, H. Cheng, L. Jiang and L. Qu, *Energy Environ. Sci.*, 2016, **9**, 912–916.
11. K. Liu, P. Yang, S. Li, J. Li, T. Ding, G. Xue, Q. Chen, G. Feng and J. Zhou, *Angew. Chem. Int. Ed.*, 2016, **55**, 8003–8007.
12. M. Li, L. Zong, W. Yang, X. Li, J. You, X. Wu, Z. Li and C. Li, *Adv. Funct. Mater.*, 2019, **29**, 1901798.
13. J. Eun and S. Jeon, *Nano Energy*, 2022, **92**, 106772.
14. T. Xu, X. Ding, Y. Huang, C. Shao, L. Song, X. Gao, Z. Zhang and L. Qu, *Energy Environ. Sci.*, 2019, **12**, 972–978.
15. J. Xue, F. Zhao, C. Hu, Y. Zhao, H. Luo, L. Dai and L. Qu, *Adv. Funct. Mater.*, 2016, **26**, 8784–8792.
16. Z. Luo, C. Liu and S. Fan, *Nano Energy*, 2019, **60**, 371–376.
17. R. Zhu, Y. Zhu, F. Chen, R. Patterson, Y. Zhou, T. Wan, L. Hu, T. Wu, R. Joshi, M. Li, C. Cazorla, Y. Lu, Z. Han and D. Chu, *Nano Energy*, 2022, **94**, 106942.
18. Y. Huang, H. Cheng, C. Yang, H. Yao, C. Li and L. Qu, *Energy Environ. Sci.*, 2019, **12**, 1848–1856.
19. H. Wang, H. Cheng, Y. Huang, C. Yang, D. Wang, C. Li and L. Qu, *Nano Energy*, 2020, **67**, 104238.
20. H. Wang, Y. Sun, T. He, Y. Huang, H. Cheng, C. Li, D. Xie, P. Yang, Y. Zhang and L. Qu, *Nat. Nanotechnol.*, 2021, **16**, 811–819.
21. J. Bai, Y. Huang, H. Wang, T. Guang, Q. Liao, H. Cheng, S. Deng, Q. Li, Z. Shuai and L. Qu, *Adv. Mater.*, 2022, **34**, 2103897.
22. D. Shen, M. Xiao, G. Zou, L. Liu, W. W. Duley and Y. Zhou, *Adv. Mater.*, 2018, **30**, 1705925.
23. W. Zhao, F. Zhang, X. Dai, W. Jin, L. Xiang, J. Ding, X. Wang, Y. Wan, H. Shen, Z. He, J. Wang, X. Gao, Y. Zou, C. A. Di and D. Zhu, *Adv. Mater.*, 2020, **32**, 2000273.
24. S. Hong, G. Zou, H. Kim, D. Huang, P. Wang and H. N. Alshareef, *ACS Nano*, 2020, **14**, 9042–9049.

25. C. Han, X. Qian, Q. Li, B. Deng, Y. Zhu, Z. Han, W. Zhang, W. Wang, S. Feng, G. Chen and W. Liu, *Science*, 2020, **368**, 1091–1098.
26. Y. T. Malik, Z. A. Akbar, J. Y. Seo, S. Cho, S. Y. Jang and J. W. Jeon, *Adv. Energy Mater.*, 2021, **12**, 2103070.
27. B. Yu, J. Duan, H. Cong, W. Xie, R. Liu, X. Zhuang, H. Wang, B. Qi, M. Xu, Z. Wang and J. Zhou, *Science*, 2020, **370**, 342–346.
28. G. Li, D. Dong, G. Hong, L. Yan, X. Zhang and W. Song, *Adv. Mater.*, 2019, **31**, 1901403.
29. J. Duan, G. Feng, B. Yu, J. Li, M. Chen, P. Yang, J. Feng, K. Liu and J. Zhou, *Nat. Commun.*, 2018, **9**, 5146.
30. H. Zhou, T. Yamada and N. Kimizuka, *J. Am. Chem. Soc.*, 2016, **138**, 10502–10507.
31. P. F. Salazar, S. T. Stephens, A. H. Kazim, J. M. Pringle and B. A. Cola, *J. Mater. Chem. A*, 2014, **2**, 20676–20682.
32. K. Kim and H. Lee, *Phys. Chem. Chem. Phys.*, 2018, **20**, 23433–23440.
33. M. A. Lazar, D. Al-Masri, D. R. MacFarlane and J. M. Pringle, *Phys. Chem. Chem. Phys.*, 2016, **18**, 1404–1410.
34. R. Hu, B. A. Cola, N. Haram, J. N. Barisci, S. Lee, S. Stoughton, G. Wallace, C. Too, M. Thomas, A. Gestos, M. E. dela Cruz, J. P. Ferraris, A. A. Zakhidov and R. H. Baughman, *Nano Lett.*, 2010, **10**, 838–846.
35. T. Kang, S. Fang, M. E. Kozlov, C. S. Haines, N. Li, Y. Kim, Y. Chen and R. H. Baughman, *Adv. Funct. Mater.*, 2012, **22**, 477–489.
36. M. S. Romano, N. Li, D. Antiohos, J. M. Razal, A. Nattestad, S. Beirne, S. Fang, Y. Chen, R. Jalili, G. G. Wallace, R. Baughman and J. Chen, *Adv. Mater.*, 2013, **25**, 6602–6606.
37. H. Im, T. Kim, H. Song, J. Choi, J. Park, R. O. Robles, H. Yang, K. D. Kihm, R. H. Baughman, H. Lee, T. Kang and Y. Kim, *Nat. Commun.*, 2016, **7**, 10600.
38. L. Zhang, T. Kim, N. Li, T. Kang, J. Chen, J. M. Pringle, M. Zhang, A. H. Kazim, S. Fang, C. Haines, D. Al-Masri, B. A. Cola, J. M. Razal, J. Di, S. Beirne, D. R. MacFarlane, A. G. Martin, S. Mathew, Y. Kim, G. Wallace and R. H. Baughman, *Adv. Mater.*, 2017, **29**, 1605652.
39. O. Bubnova, Z. U. Khan, A. Malti, S. Braun, M. Fahlman, M. Berggren and X. Crispin, *Nat. Mater.*, 2011, **10**, 429–433.
40. G. Kim, L. Shao, K. Zhang and K. P. Pipe, *Nat. Mater.*, 2013, **12**, 719–723.
41. P. Yang, K. Liu, Q. Chen, X. Mo, Y. Zhou, S. Li, G. Feng and J. Zhou, *Angew. Chem. Int. Ed.*, 2016, **128**, 12229–12232.
42. J. Duan, B. Yu, K. Liu, J. Li, P. Yang, W. Xie, G. Xue, R. Liu, H. Wang and J. Zhou, *Nano Energy*, 2019, **57**, 473–479.
43. T. Li, X. Zhang, S. D. Lacey, R. Mi, X. Zhao, F. Jiang, J. Song, Z. Liu, G. Chen, J. Dai, Y. Yao, S. Das, R. Yang, R. M. Briber and L. Hu, *Nat. Mater.*, 2019, **18**, 608–613.

44. D. Zhao, A. Martinelli, A. Willfahrt, T. Fischer, D. Bernin, Z. U. Khan, M. Shahi, J. Brill, M. P. Jonsson, S. Fabiano and X. Crispin, *Nat. Commun.*, 2019, **10**, 1093.
45. B. Chen, Q. Chen, S. Xiao, J. Feng, X. Zhang and T. Wang, *Sci. Adv.*, 2021, **7**, eabi7233.
46. T. Kim, J. Lee, G. Lee, H. Yoon, J. Yoon, T. Kang and Y. Kim, *Nano Energy*, 2017, **31**, 160–167.
47. L. Jin, G. W. Greene, D. R. MacFarlane and J. M. Pringle, *ACS Energy Lett.*, 2016, **1**, 654–658.
48. N. Komatsu, Y. Ichinose, O. S. Dewey, L. W. Taylor, M. A. Trafford, Y. Yomogida, G. Wehmeyer, M. Pasquali, K. Yanagi and J. Kono, *Nat. Commun.*, 2021, **12**, 4931.
49. A. J. deBethune, T. S. Licht and N. Swendeman, *J. Electrochem. Soc.*, 1959, **106**, 616–625.
50. S. Arrhenius, *Z. Phys. Chem.*, 1889, **4U**, 96–116.
51. A. L. Buck, *J. Appl. Meteorol. Climatol.*, 1981, **20**, 1527–1532.
52. G. Kresse and J. Furthmüller, *Phys. Rev. B*, 1996, **54**, 11169.
53. J. P. Perdew, K. Burke and M. Ernzerhof, *Phys. Rev. Lett.*, 1996, **77**, 3865–3868.
54. S. Plimpton, *J. Comput. Phys.*, 1995, **117**, 1–19.
55. C. C. Battaile, *Comput. Method. Appl. M.*, 2008, **197**, 3386–3398.
56. A. B. Bortz, M. H. Kalos and J. L. Lebowitz, *J. Comput. Phys.*, 1975, **17**, 10–18.
57. D. T. Gillespie, *J. Phys. Chem.*, 1977, **81**, 2340–2361.
58. X. Liu, H. Gao, J. E. Ward, X. Liu and J. Yao, *Nature*, 2020, **578**, 550–554.
59. S. Kim, K. Lee, H. A. Mun, H. Kim, S. Hwang, J. W. Roh, D. Yang, W. H. Shin, X. Li, Y. Lee, G. J. Snyder and S. Kim, *Science*, 2015, **348**, 109–114.